



Article

# Computational Investigation of the Mechanical Response of a Bioinspired Nacre-like Nanocomposite under Three-Point Bending

Xingzi Yang <sup>†</sup>, Md Jalal Uddin Rumi <sup>†</sup> and Xiaowei Zeng <sup>\*</sup>

Department of Mechanical Engineering, University of Texas at San Antonio, San Antonio, TX 78249, USA; xingzi.yang@utsa.edu (X.Y.); mdjalaluddin.rumi@utsa.edu (M.J.U.R.)

<sup>\*</sup> Correspondence: xiaowei.zeng@utsa.edu; Tel.: +1-210-458-7698

<sup>†</sup> These authors contributed equally to this work.

**Abstract:** Natural biological nanocomposites, like nacre, demonstrate extraordinary fracture toughness, surpassing their base materials, attributed to their intricate staggered hierarchical architectures integrating hard and soft phases. The enhancement of toughness in these composites is often linked to the crack-deflection mechanism. Leveraging the core design principles that enhance durability, resilience, and robustness in organic materials, this paper describes the use of computational modeling and simulation to perform a three-point bending test on a 3D staggered nanocomposite intentionally crafted to mimic the detailed microstructure of nacre. We adopted a previously proposed interfacial zone model that conceptualizes the “relatively soft” layer as an interface between the “hard” mineral tablets and the microstructure’s interlayer spaces to examine how the microstructure and interface characteristics affect the mechanical responses and failure mechanisms. By comparing the model’s predictions with experimental data on natural nacre, the simulations unveil the mechanisms of tablet separation through adjacent layer sliding and crack deflection across interfacial zones. This study offers a robust numerical method for investigating the fracture toughening mechanisms and damage evolution and contributes to a deeper understanding of the complex interplays within biomimetic materials.

**Keywords:** cohesive zone model; three-point bending; bioinspired nanocomposite; finite-element simulation; mechanical property



**Citation:** Yang, X.; Rumi, M.J.U.; Zeng, X. Computational Investigation of the Mechanical Response of a Bioinspired Nacre-like Nanocomposite under Three-Point Bending. *J. Compos. Sci.* **2024**, *8*, 173. <https://doi.org/10.3390/jcs8050173>

Academic Editor: Francesco Tornabene

Received: 6 April 2024

Revised: 20 April 2024

Accepted: 3 May 2024

Published: 7 May 2024



**Copyright:** © 2024 by the authors. Licensee MDPI, Basel, Switzerland. This article is an open access article distributed under the terms and conditions of the Creative Commons Attribution (CC BY) license (<https://creativecommons.org/licenses/by/4.0/>).

## 1. Introduction

The exceptional mechanical properties of biological nanocomposites, including bone [1,2] and mollusk shells [3], derive from the sophisticated integration of hard and soft phases within their structures. Notably, these materials feature a staggered “brick and mortar” microstructure, where mineral inclusions are aligned with the load directions and bonded by bio-polymeric layers [4]. For example, nacre in mollusk shells comprises about ~95 wt% aragonite tablets in a staggered arrangement, connected by ~5 wt% biopolymeric interfaces [5]. Similarly, bone displays staggered structures at different scales, including osteons segmented by cement lines and composed of unidirectionally aligned collagen fibers. This staggered configuration is a common architectural theme across diverse load-bearing biological materials, indicating an evolutionary advantage in providing optimal stiffness, strength, and toughness [6–10]. Inspired by these natural structures, considerable progress has been made in synthesizing bioinspired composites through freeze-casting, self-assembly, and controlled mineralization [11–14]. These techniques endeavor to mimic the natural microstructures of nacre, although perfectly periodic staggered arrangements are typically only feasible on a larger scale in engineered materials [15–18].

The mechanical integrity of staggered biological nanocomposites is primarily dictated by the dynamic interaction of mineral inclusions gliding past each other, facilitated by the

compliance of softer interfacial layers. This interaction induces nonlinear deformations and activates key toughening mechanisms, such as crack deflection and the interlocking of mineral components within different layers [2,19,20]. Researchers have proposed various theoretical and numerical models to estimate these composites' stiffness, strength, and toughness, considering their unique microstructural characteristics and the distinct properties of the hard and soft phases. These models frequently employ compact, two-dimensional representative volume elements (RVEs) to finely tune the material's modulus, strength, and energy absorption properties [2,5,6,9,21–23]. However, these RVE-based models often assume perfect periodicity and uniform failure across all components. This simplification does not account for the microstructural variations and compositional heterogeneity inherent in biological and bioinspired materials [5,24,25]. Recent advancements in modeling have integrated larger numbers of tablets to represent better structure–property relationships over more substantial volumes [3,26–29]. However, these models also face limitations, such as focusing only on elastic responses and brittle failure. Researchers have proposed more sophisticated approaches like finite-element methods to address these challenges, despite their computational intensity [3,26,30–32]. Additionally, discrete-element models offer computational efficiency, but are less commonly used [28,29,33,34]. Further studies using models like shear lag for stress transfer [5,21,35] and bilinear cohesive zone models for various loading conditions [36] have enriched our understanding. Previously, the authors of this present study conducted a detailed analysis of thin plate structures' behavior and failure modes in nacre-mimetic nanocomposites under tensile and compressive loads. This research particularly examined the impact of the junction and interlayer organic interfaces on managing tensile instability and compressive buckling phenomena in these lean composite systems [37]. These computational explorations underscore the deliberate architectural integration of soft and stiff phases as a crucial strategy for enhancing the mechanical properties of nacre-like biological nanocomposites.

Despite significant advances in research on nacre-mimetic materials, a comprehensive understanding of their mechanical behavior still needs to be discovered due to their complex microstructures and the multiscale nature of their operating mechanisms. The lack of comprehensive 3D computational models, essential for elucidating deformation dynamics, failure mechanisms, and the correlation between structure and properties and evaluating the function of the organic interfacial zones, significantly hampers the formulation of accurate design principles. This limitation obstructs progress in creating damage-tolerant materials, which are essential for applications in engineering and biomedicine. The current study presents a computational approach designed to model and simulate a three-point bending test on a 3D staggered nanocomposite that closely mimics the microstructure of nacre to evaluate the mechanical response and damage evaluation, thereby addressing existing gaps in our understanding. The model developed in this research features a configuration of randomly positioned hard mineral tablets, which are bonded together by slender, pliable interfacial zones at the microstructure's junctions and among different layers. Utilizing a cohesive zone modeling strategy [38] that employs generalized traction–separation laws, this approach adeptly captures the complex behaviors at the organic matrix interfaces. The simulations' results shed light on how the composite's microstructural arrangement and interfacial characteristics affect its bending response, offering profound insights into the design principles and the mechanical dynamics of bioinspired staggered composites.

## 2. Computational Model and FEM Implementation

### 2.1. Geometric Model of Staggered Nanocomposite

The model adopted in this study emulates the intricate ultrastructure of nacre, a naturally engineered structural composite renowned for its multilayered staggered microstructure. The composite comprises polygonal, high-aspect-ratio tablets of aragonite ( $\text{CaCO}_3$ ) crystals, linked via thin layers of organic biopolymers functioning as a cohesive zone essential for maintaining structural integrity. Initially, a 2D array of randomly positioned polygon-shaped  $\text{CaCO}_3$  crystals was constructed using the Centroidal Voronoi Tessellation

(CVT) method. This was followed by the integration of a 20 nm thin organic interface interposed between the  $\text{CaCO}_3$  crystals by methodically drawing back the edges of each crystal towards their centroids by 10 nm (Figure 1). For an in-depth understanding of the implementation of the CVT method, readers are referred to a previous work by the authors [39].

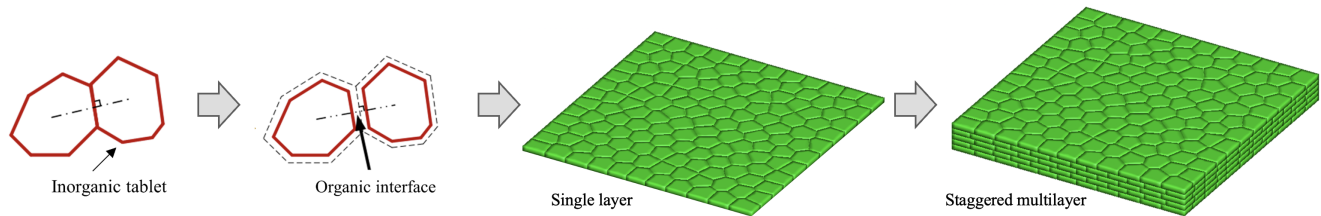


**Figure 1.** Fabrication process of the 3D staggered composite model: initial 2D model creation using CVT, development of the interfacial zone by modifying Voronoi cell boundaries, and assembly of varied layers to construct the final 3D composite.

Initially, the 2D model underwent an orthogonal extrusion process to establish a foundational layer of the mineral–organic nanocomposite with the thickness set at 500 nm. This procedure was systematically repeated to fabricate a sequence of five layers, each distinguished by a unique pattern of mineral tablets determined by differing Voronoi seed distributions. These individual layers were subsequently assembled to form a comprehensive 3D multilayered nanocomposite. To ensure structural integrity and enhance interlayer adhesion, a 20 nm thick organic matrix was interleaved between consecutive layers (Figure 2). Empirical assessments and convergence analyses determined that a minimum of 100 grains per layer was necessary to guarantee robust and consistent results [40], with our model incorporating approximately 144  $\text{CaCO}_3$  grains per layer. Consistent with established literature, the thickness of both the junction and interlayer interfaces was uniformly maintained at 20 nm [41–44], corresponding to an organic matrix volume fraction of about 5% [3,45]. The overall dimensions of the specimen were defined as 8400 nm × 8400 nm × 2500 nm.

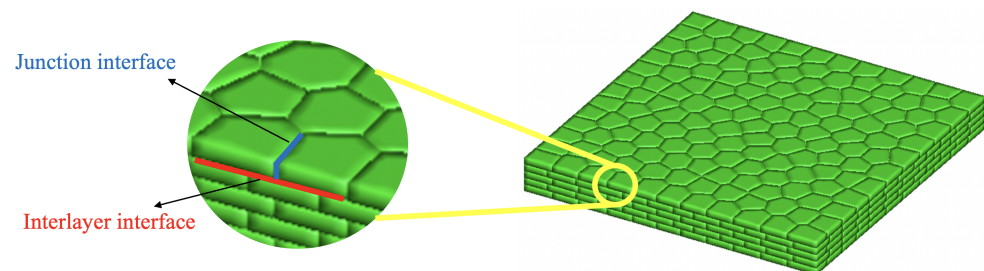


**Figure 2.** Schematic representation of granular nanocomposite: microstructural details of staggered composite and interfaces between grains and interlayers.

## 2.2. Interfacial Zone Modeling Using Cohesive Zone Model

The cohesive zones enveloping the mineral tablets manifest as junction and interlayer interfacial zones, as depicted in Figure 2. Despite the organic matrix’s relative weakness and minor volumetric contribution to the nanocomposite, it significantly influences the composite’s mechanical properties. During tablet debonding and sliding, the matrix can sustain extensive normal and shear deformations [46]. The deformation behaviors of the interfaces, owing to their slender profile, are aptly characterized by a generalized interfacial zone model [38]. The mechanics of the interface are governed by traction–separation relations, detailed in Figure 3. These relations outline three critical phases in the normal traction–separation law: the compressive contact stage ( $0 \sim \delta_0$ ), the elastic phase ( $\delta_0 \sim \delta_{dn}$ ),

and the damage phase ( $\delta_{dn} \sim \delta_{fn}$ ). The shear traction–separation law mirrors these stages, showing symmetric behavior in both directions.

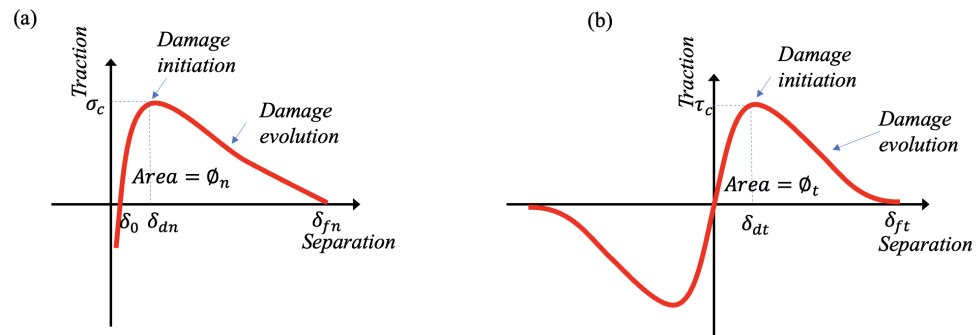


**Figure 3.** Representative traction–separation curves for interfacial behaviors: (a) normal direction and (b) shear direction.

To effectively model the cohesive interactions within a staggered composite, it is crucial to acknowledge that normal and shear forces do not necessarily exert coupled effects. For instance, unclamping and unfolding in collagen fibrils during stretching may occur without significant shear interactions [47]. Consequently, an uncoupled cohesive zone model was employed to differentiate the interactions at the junction and interlayer interfaces [38,48]. The governing traction–separation laws for these interfaces are articulated as follows:

$$T_n = \begin{cases} \sigma_c \left( \frac{\Delta_n - \delta_0}{\delta_{dn} - \delta_0} \right) \left[ e^{1 - \frac{\Delta_n - \delta_0}{\delta_{dn} - \delta_0}} \right]^{q_n} & \Delta_n \leq \delta_{dn} \\ \sigma_c \left( \frac{\delta_{fn} - \Delta_n}{\delta_{fn} - \delta_{dn}} \right)^{p_n} & \delta_{dn} < \Delta_n < \delta_{fn} \\ 0 & \Delta_n \geq \delta_{fn} \end{cases} \quad (1)$$

$$T_t = \begin{cases} \tau_c \left( \frac{\Delta_t}{\delta_{dt}} \right) \left[ e^{\frac{1}{2} - \frac{\Delta_t^2}{2\delta_{dt}^2}} \right]^{q_t} & 0 \leq |\Delta_t| \leq \delta_{dt} \\ \tau_c \frac{\Delta_t}{|\Delta_t|} \left( \frac{\delta_{ft} - |\Delta_t|}{\delta_{ft} - \delta_{dt}} \right)^{p_t} & \delta_{dt} < |\Delta_t| < \delta_{ft} \\ 0 & |\Delta_t| \geq \delta_{ft} \end{cases} \quad (2)$$

The formulations presented in Equations (1) and (2) incorporate six parameters ( $\sigma_c$ ,  $\delta_0$ ,  $\delta_{dn}$ ,  $\delta_{fn}$ ,  $q_n$ , and  $p_n$ ) that dictate the normal traction behavior and five parameters ( $\tau_c$ ,  $\delta_{dt}$ ,  $\delta_{ft}$ ,  $q_t$ , and  $p_t$ ) that control shear traction responses. This parameterization provides the necessary flexibility to simulate varying interfacial properties and responses accurately. Interface toughness ( $\varnothing_n$ ,  $\varnothing_t$ ) can be quantified from the integrated area beneath the traction–separation curves, where  $\sigma_c$  and  $\tau_c$  signify the cohesive strengths in the normal and shear directions, respectively. The parameters  $\delta_{dn}$  and  $\delta_{dt}$  represent critical separations for initiating damage. In contrast,  $\delta_{fn}$  and  $\delta_{ft}$  are the separations at failure in the normal and shear directions. The initial equilibrium position,  $\delta_0$ , reflects the organic interface thickness typical in staggered composites. Shape parameters ( $q_n$ ,  $p_n$ ,  $q_t$ , and  $p_t$ ) were introduced to capture various damage degradation behaviors—concave, convex, or linear—across the traction–separation curve. The following equations quantitatively define the stiffness of the interface at its equilibrium position:

$$K_n = \left. \frac{dT_n}{d\Delta_n} \right|_{\Delta_n = \delta_0} = \frac{\sigma_c e^{q_n}}{\delta_{dn} - \delta_0} \quad (3)$$

$$K_t = \left. \frac{dT_t}{d\Delta_t} \right|_{\Delta_t = 0} = \frac{\tau_c e^{\frac{q_t}{2}}}{\delta_{dt}} \quad (4)$$

Equations (3) and (4) precisely describe how rigid the interface remains when subjected to external forces, reflecting its ability to resist deformation under load. As outlined in these equations, a reduction in the parameters  $(\delta_{dn} - \delta_0)$  or  $\delta_{dt}$  correlates with an increase in the stiffness of the interface in the normal or tangential directions, respectively. This relationship underscores the mechanical responsiveness of the interface under varying strain conditions.

The interfacial toughness, represented by the area under the traction–separation curve, indicates the material’s ability to dissipate energy during failure and offers insights into its resilience under stress. The calculations for normal and shear interfacial toughness were computed as follows:

$$\varnothing_n = \int_{\delta_0}^{\delta_{dn}} T_n d\delta \tag{5}$$

$$\varnothing_t = \int_0^{\delta_{dt}} T_t d\delta \tag{6}$$

Adopting the cohesive zone model has been instrumental in elucidating the failure mechanisms in polycrystalline composite materials, effectively capturing the progression of material failure across diverse studies [49–53]. This methodological approach allows for a nuanced understanding of the interfacial dynamics and their critical role in the structural integrity of composite materials.

### 2.3. Material Properties

Multiple stratified layers constitute the interfacial regions within nacre, each embedded with polymers characterized by unique modular molecular architectures. These polymers, operating at the nanoscale, exhibit complex behaviors that pose significant challenges for precise experimental characterization [44,54]. In this study, we have modeled the mechanical properties of the interfacial zones using a simplified approach governed by traction–separation laws. These laws are based on parameters derived from an extensive review of experimental and simulation studies focused on nacre’s organic phase [3,42,54–56].

The biopolymer layers at the junctions and within the interlayer matrices of nacre, despite their minimal thickness, can endure significant mechanical deformation. This resilience is enabled by the sequential unfolding of molecular modules, a phenomenon substantiated by experimental evidence demonstrating substantial elongation of these molecules [54]. Moreover, the interfaces between these organic layers and adjacent mineral components permit a degree of slippage, thereby augmenting the overall deformability of the composite [46]. Observations from several studies indicate that these interfaces exhibit a marked and sustained plateau phase following yield, highlighting their distinctive mechanical characteristics [3,55].

In our model, the interfacial zone is assumed to exhibit elastic–perfectly plastic behavior. The critical normal separation at the interface  $(\delta_{dn} - \delta_0)$  was established at 0.6 nm, and the normal failure separation  $(\delta_{fn} - \delta_0)$  was set to 50 nm, following Barthelat’s approach [3]. Given the lack of empirical data on shear behavior at interfaces, we posited that shear behavior would mirror that observed in the normal dimension, setting both the critical shear separation,  $\delta_{dt}$ , and the failure shear separation,  $\delta_{ft}$ , at 0.6 nm and 50 nm, respectively. The strengths in the normal and shear directions were defined as  $\sigma_c = 40$  MPa and  $\tau_c = 40$  MPa, congruent with documented experimental outcomes [42,55–57]. The detailed specifications of these interface parameters are systematically presented in Table 1.

**Table 1.** Parameters for cohesive modeling of interfacial zones with elastic–perfectly plastic behavior.

$\sigma_c$ (MPa)	$\delta_{dn} - \delta_0$ (nm)	$\delta_{fn} - \delta_0$ (nm)	$p_n$	$q_n$	$\tau_c$ (MPa)	$\delta_{dt}$ (nm)	$\delta_{ft}$ (nm)	$p_t$	$q_t$
40	0.6	50	1	0	40	0.6	50	1	0

Due to the paucity of comprehensive experimental data, this study assigns uniform material properties to the junction and interlayer interfaces in nacre. However, more nuanced representations might consider variations between these interfaces influenced by factors like mineral bridges and tablet waviness. Utilizing values from the literature for aragonite crystal [27,36,43,58,59], the material properties of CaCO<sub>3</sub> were specified as follows: Young’s modulus  $E = 106$  GPa, Poisson’s ratio  $\nu = 0.3$ , and mineral density  $\rho = 3190$  kg/m<sup>3</sup>.

2.4. FEM Implementation of the Cohesive Zone Model

The finite-element (FE) model-based simulation was conducted by using a custom-designed FORTRAN code. In this framework, conventional principles were adhered to while opting to exclude body forces for simplicity. The fundamental equation governing the finite-element formulation, based on the principle of virtual work, is expressed as:

$$\int_{\Omega} \rho \ddot{\mathbf{u}} \cdot \delta \mathbf{u} d\Omega = \int_{\Gamma_{\text{ext}}} \bar{\mathbf{T}} \cdot \delta \mathbf{u} dS + \int_{\Gamma_{\text{inter}}} \mathbf{T}^{\text{inter}} \cdot \delta \Delta dS - \int_{\Omega} \mathbf{P} : \delta \mathbf{F} d\Omega$$

where  $\Omega$  denotes the volume of the element in its reference configuration and  $\Gamma_{\text{inter}}$  and  $\Gamma_{\text{ext}}$  denote the interface and external traction boundaries, respectively. The first Piola–Kirchhoff stress tensor is represented by  $\mathbf{P}$ , and  $\mathbf{F}$  is the deformation gradient tensor. The term  $\Delta$  encapsulates the displacement jump across interfaces;  $\bar{\mathbf{T}}$  is the vector of external tractions;  $\mathbf{T}^{\text{inter}}$  represents the interfacial bonding traction.  $\rho$  is the density of the material in its reference state.

The Newmark  $\beta$  method was employed for temporal discretization, specifically with parameters  $\beta = 0$  and  $\gamma = 0.5$ , to facilitate explicit time integration as detailed in the literature [60]. This choice supports the dynamic analysis within the simulation framework, accommodating the computational model’s requirements for accuracy in transient response evaluations.

The mechanical response of junction and interlayer interfacial zones within the model are dictated by the previously outlined traction–separation laws, ensuring a robust representation of physical interactions at the microstructural level. These cohesive zones were incorporated in the FEM implementation following the standard procedures described in [38]. The CaCO<sub>3</sub> grains, configured in polygonal shapes across all layers, were meshed using 86,994 wedge elements. Figure 4 illustrates a detailed view of the specimen after meshing. This detailed meshing strategy enhances the model’s capacity to accurately simulate the complex mechanical behaviors characteristic of biological composites under varied loading conditions.

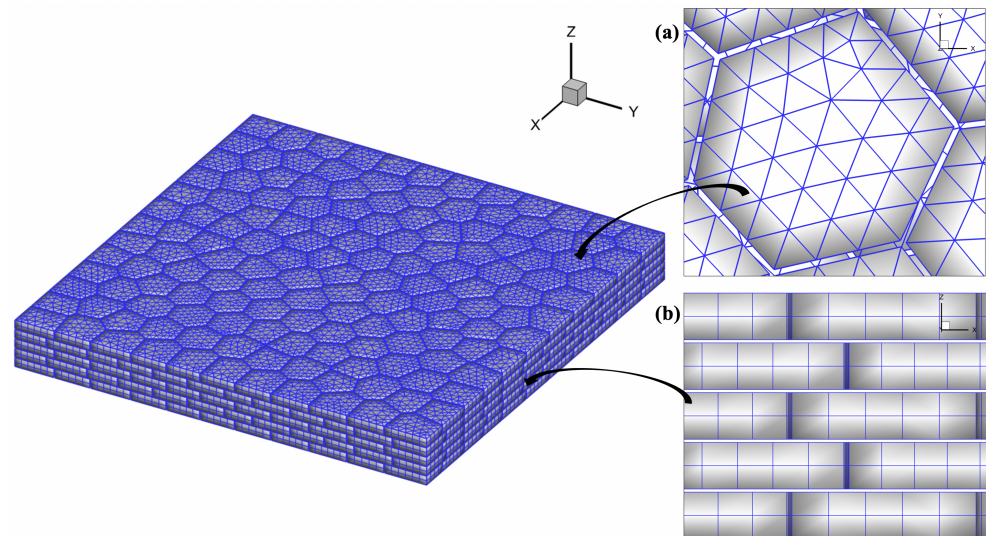


**Figure 4.** Microstructural meshing of the specimen: (a) single grain meshing detail and (b) layer-by-layer meshing configuration.

### 2.5. Loading and Boundary Conditions

We set up the proposed model to simulate a three-point bending test to evaluate the system's mechanical response and damage evolution. The loadings and boundary conditions setup for the FEA implementation are depicted in Figure 5. The setup includes two rollers in contact with the bottom layer of the specimen, which were held stationary (Figure 5a), while a displacement was imposed on the roller contacting the top layer at the center (Figure 5b). This study incorporated various displacement velocity boundary conditions along the negative Z-axis across different simulations. The results presented herein correspond to a simulation implemented with a displacement loading velocity of 63 nm/s. The model's convergence was verified by setting the time step at 30  $\mu$ s.

While this study concentrated on bending loads to examine mechanical responses and deformation in nacre, it recognizes the relevance of other significant loading modes, including tensile and compressive stresses, in-plane shear, and out-of-plane deformation. These modes, which possess considerable engineering relevance, were not examined in this study but are documented in the literature [37,61–66].

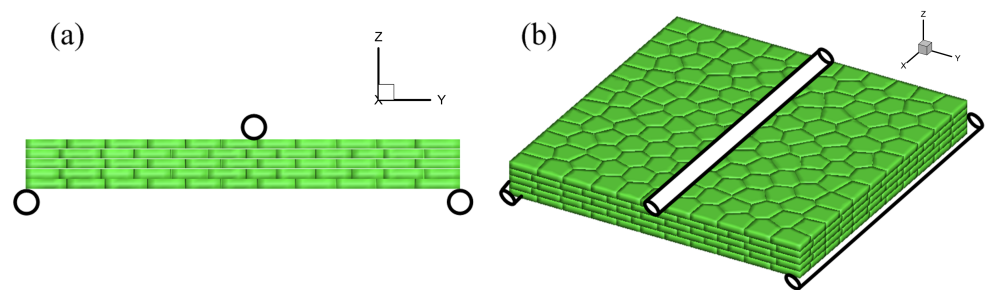


**Figure 5.** Schematic representation of the three-point bending test setup in the simulation: (a) front view and (b) 3D view of the setup.

## 3. Results and Discussion

Numerical simulations have been meticulously executed on the proposed geometric model to explore its mechanical response and the underlying failure mechanisms when subjected to three-point bending. The findings from these simulations are described in the subsequent sections.

### 3.1. Mechanical Response

The 3D view of the three-point bending simulation, as depicted in Figure 6, illustrates the evolution of the bending stress distribution along the y-axis. Initially, the stress distribution away from the loading sites remains notably uniform in the elastic deformation phase before nanocracks appear (Figure 6a,b). This uniformity signals the integral participation of mineral tablets in bearing the applied load, highlighting the interfacial zones' critical function in transmitting stress across mineral components, thereby maximizing the structural benefits of the stiff mineral tablets. Despite the interfacial critical strength being limited to 40 MPa, the mineral phase experienced a significantly elevated stress level of approximately 350 MPa at the onset of microcrack initiation. This increased stress is attributed to the interfaces effectively distributing forces across the hard mineral grains.

As the applied load intensifies, initial damage at different interfacial zones begins, releasing localized stress around the damage sites (Figure 6c). Subsequent stretching results in crack growth and coalescence, eventually reaching the final failure stage (Figure 6d–f). The notable range in deformation from the initial crack formation ( $d_f = 226.8$  nm) to final failure ( $d_f = 756$  nm) highlights the interfaces' effectiveness in delaying final crack progression by deflecting the crack path and reducing stress concentration at the crack tip. For an in-depth analysis of the intralayer dynamics, Figure 7 provides a detailed view of the specimen's bottom layer. At the onset of crack initiation, localized stress concentrations emerge at various sites (Figure 7a). Crack nucleation follows, involving the formation of small cracks at the

sites with a high-stress concentration from opening the interfacial zones of the materials at the microscopic level (Figure 7b). These small microscopic cracks coalesce to form a larger, macroscopic crack propagating through the damaged interfacial zones (Figure 7c), leading to a complete failure in a “zig-zag” fashion without rupturing the mineral tablets (Figure 7d). These investigations underscore the critical role of the mode of junction interface separation as the dominant mechanism dictating the model’s deformation and fracture behavior under bending stress and align with the experimental studies [67–69].

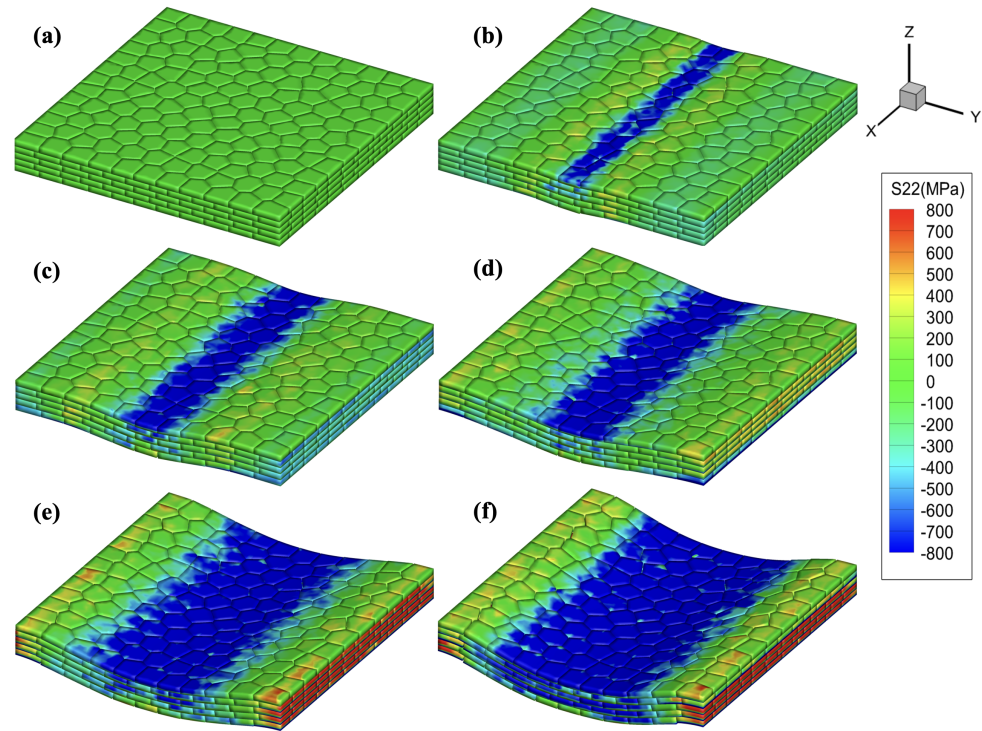


**Figure 6.** Sequential stress distribution snapshots ( $\sigma_{22}$ ) during the simulation: (a)  $d_f = 0.0$  nm (initial stage), (b)  $d_f = 83.16$  nm (initial loading stage), (c)  $d_f = 226.8$  nm (microcrack initiation), (d)  $d_f = 393.12$  nm (crack growth), (e)  $d_f = 574.56$  nm (crack coalescence), and (f)  $d_f = 756$  nm (final failure stage).

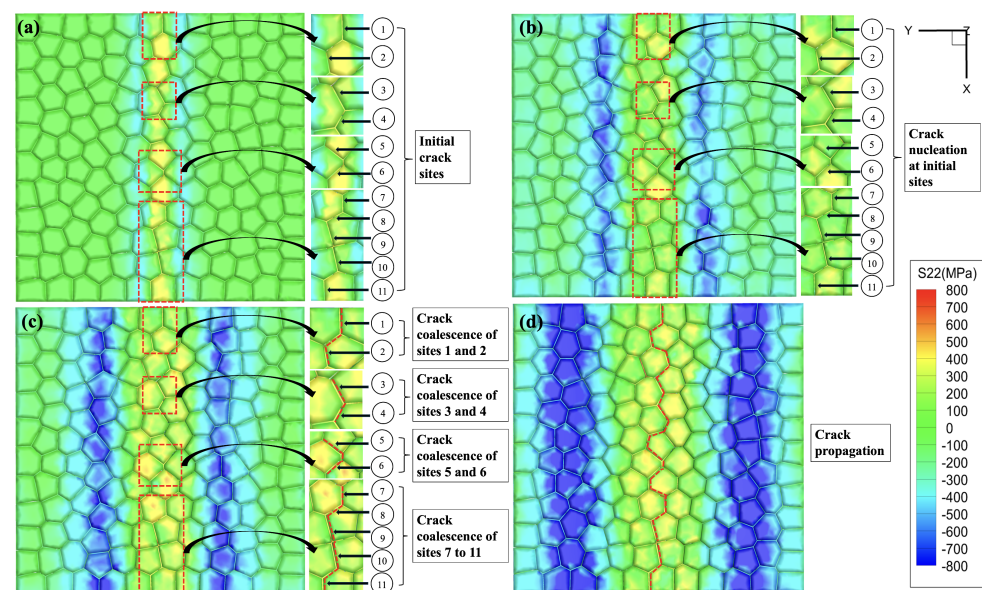


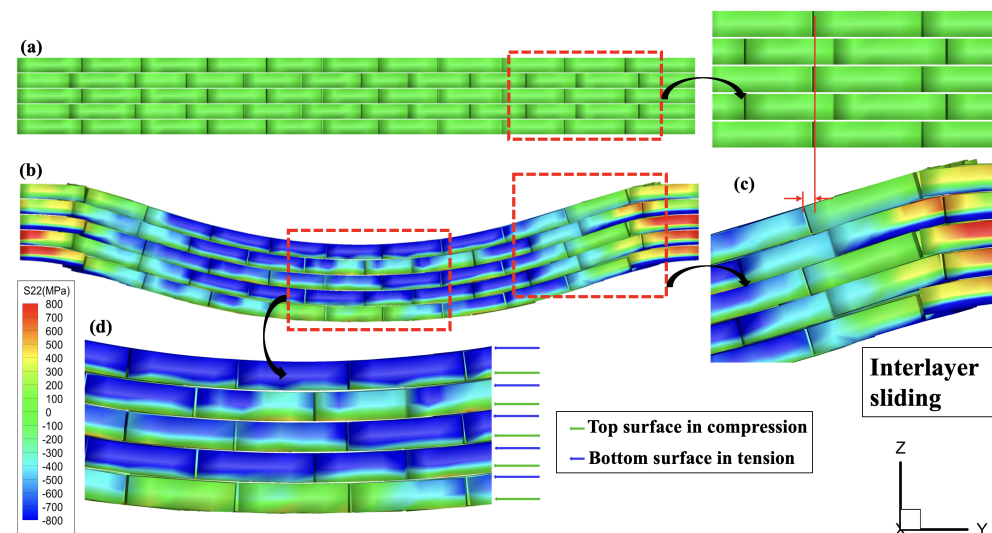
**Figure 7.** Detailed analysis of the bottom layer in Figure 6: (a) initial crack sites exhibiting high-stress concentration, (b) microcrack nucleation along interfacial zones at initial crack sites, (c) coalescence of microcracks from various sites, and (d) crack propagation along interfacial zones.

### 3.2. Failure Mechanism and Fracture Morphology

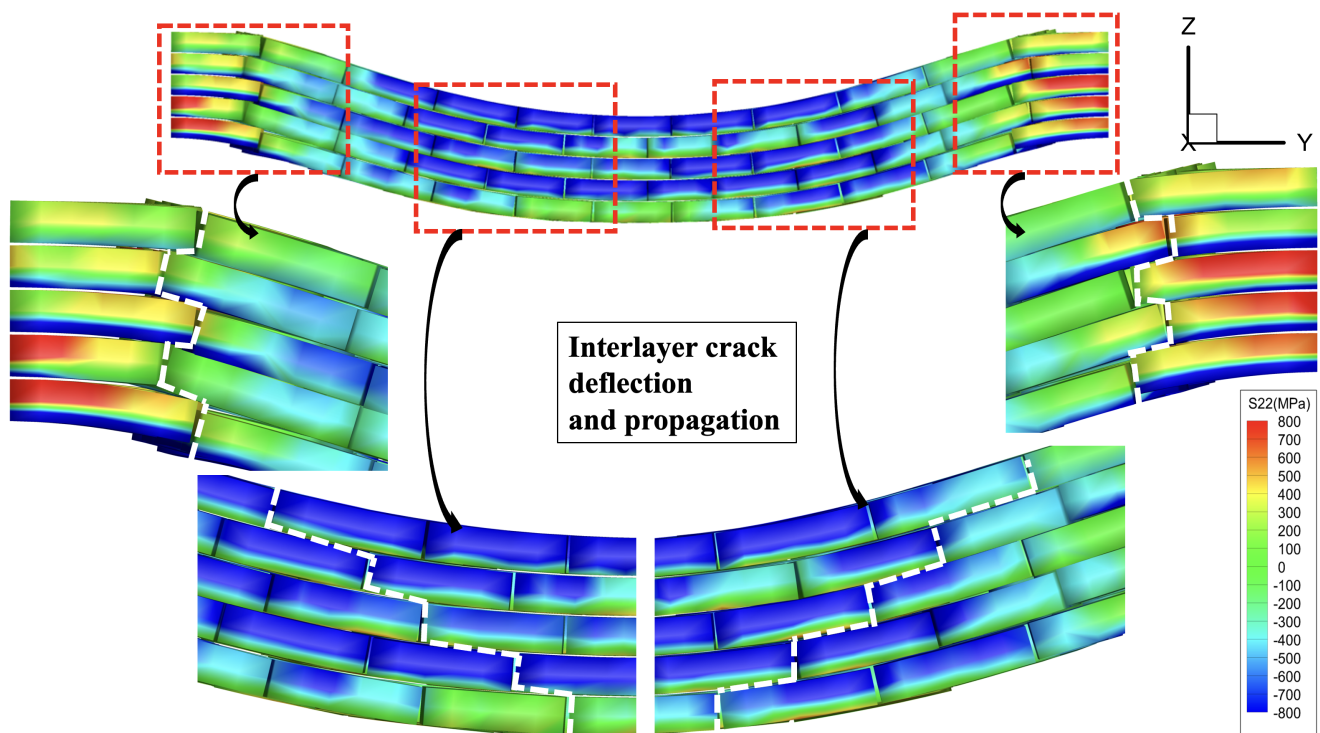
Crack propagation and evolution within the model did not manifest as the instantaneous phenomena typically observed in brittle materials such as nacre's main constituent, aragonite. Instead, the model's interfacial zones facilitated junction and interlayer sliding of mineral tablets, accommodating extensive deformations. Figure 8 illustrates a closer look into tablets sliding among adjacent layers and the stress distribution of alternating compressive and tensile stresses within each layer of a completely fractured specimen. As the specimen deforms under bending load, the junction and interlayer mineral tablets slide referenced to their original arrangements at the preloading stage to distribute the induced bending stress throughout the specimen (Figure 8c). The stress distribution of each layer can also explain this phenomenon. Each layer slide referenced to its original arrangement experiences alternating compressive (top surface) and tensile stress (bottom surface), as illustrated in Figure 8d. Additionally, investigation on the shear stress ( $\sigma_{12}$ ) distribution along interlayer contact surfaces depicts that this value reaches a maximum of  $\sim 550$  MPa. This investigation also confirms the interlayer sliding of mineral tablets due to the excessive shear deformation of the interlayer interfacial zones.

Figure 9 outlines a detailed view of crack deflection and propagation within different layers observed under bending load. Our study reveals that nacre's crack deflection mechanism is mediated by microcracking ahead of the main crack rather than occurring directly. These microcracks alleviate local stress concentrations, enhancing nacre's resistance to crack propagation. Like other biological composites such as bone, microcracking is instrumental in facilitating crack deflection, tied to damage mechanisms near the crack tip that promote further cracking. This deflection mechanism is crucial for nacre's enhanced toughness.

Additionally, our findings contribute to understanding nacre's damage morphology, revealing that the strong bonding between organic interfaces and mineral platelets allows for microcracking and subsequent crack deflection. This process protects aragonite platelets from the propagating crack, leading to a "ragged platelet" morphology with an irregular "step-like" pattern, which increases surface roughness (Figure 9). This observation aligns with the experimental three-point bending test of nacre [67–69].



**Figure 8.** Comprehensive analysis of the specimen's front face illustrating preloading and fracture stages: (a) initial configuration of mineral tablets across different layers, (b) final configuration and stress distribution in a fully fractured specimen, (c) sliding dynamics of adjacent layers, and (d) stress distribution within a single layer.



**Figure 9.** Detailed visualization of interlayer crack deflection and propagation in the specimen.

#### 4. Future Studies and Applications

Nacre, known for its exceptionally lightweight and high-strength characteristics, has become a focal point in biomimetic materials. Driven by the micro-layered structure of nacre, researchers are actively developing artificial nacre-mimetic materials to harness these superior mechanical properties. Innovations have included models and syntheses such as dopamine cross-linked graphene oxide (GO) [70], titanic acid-functionalized GO with polyvinyl chloride (PVC) enabled by multidentate hydrogen bonding [71], supramolecular assemblies of GO [72], and GO configurations exploiting the interfacial interactions of  $\pi$ - $\pi$  stacking and hydrogen bonding [73]. Additionally, some have explored biodegradable, ultra-thin films made of polyurethane nano-cellulose/MXene/ANF/AgNPs that emulate nacre's ultrastructure [74–78]. These approaches, however, involve complex production processes and expensive testing methodologies. To evaluate the performance of these artificial nacres, our study introduces a robust numerical method to explore the fracture toughening mechanisms and damage progression in these biomimetic materials, enhancing our understanding of their intricate behaviors and allowing for the optimization of design parameters before industrial scale-up. While this research primarily addresses bending loads to study the mechanical responses and deformation mechanisms in nacre-mimetic materials, we recognize the importance of impact loading as another critical test scenario for assessing mechanical performance. However, this falls outside the scope of this paper. Previous studies have explored impact loading on natural and artificial nacre-like materials [79–81], highlighting the costly nature of experimental approaches. There is a pressing need for comprehensive numerical models capable of accurately simulating such conditions. Our team is currently developing numerical tools aimed at modeling impact loading scenarios on bioinspired nacre-mimetic materials, promising significant advancements in this area of research.

#### 5. Conclusions

This study introduces a computational model and simulation framework designed to execute a three-point bending test on a 3D staggered composite, which closely mimics the complex microstructure of nacre. By implementing an interfacial zone model, we

meticulously analyzed the behavior at both the junction and interlayer interfaces within the nanocomposite. This proposed methodology enables a comprehensive examination of its mechanical response and the underlying failure mechanisms, focusing on microstructural interactions and interface dynamics. The model revealed that the sliding motion of adjacent layers primarily drives tablet separation in the composite. At the same time, crack deflection at the interfacial zones critically influences the material's deformation and ultimate failure during bending stresses. The simulation results closely align with experimental data from natural nacre, validating the accuracy of our computational approach under analogous loading conditions. These findings highlight the critical influence of microstructural and interfacial behaviors in the mechanical performance of bioinspired multilayered nanocomposites. The developed numerical framework offers profound insights into these materials' operational mechanics and is a crucial tool for enhancing the design and optimization of advanced composite materials across diverse applications. This research makes a significant contribution to the field of materials science, particularly through its advancements in the design and analysis of bioinspired composite structures, enriching the existing body of knowledge and paving the way for future innovations in this area.

**Author Contributions:** Conceptualization, X.Z.; methodology, X.Z.; software, X.Y. and M.J.U.R.; validation, X.Y. and M.J.U.R.; formal analysis, X.Y. and M.J.U.R.; investigation, X.Y. and M.J.U.R.; resources, X.Z.; data curation, X.Y. and M.J.U.R.; writing—original draft preparation, X.Y. and M.J.U.R.; writing—review and editing, X.Z. and M.J.U.R.; visualization, X.Y. and M.J.U.R.; supervision, X.Z.; project administration, X.Z.; funding acquisition, X.Z. All authors have read and agreed to the published version of the manuscript.

**Funding:** This research was funded by a grant from the University of Texas at San Antonio, Office of the Vice President for Research.

**Institutional Review Board Statement:** Not applicable.

**Informed Consent Statement:** Not applicable.

**Data Availability Statement:** All data generated or analyzed during this study are included in this published article.

**Acknowledgments:** Valuable discussions with Liqiang Lin at Mechanical Engineering of UTSA are gratefully acknowledged.

**Conflicts of Interest:** The authors declare no conflicts of interest.

## Abbreviations

The following abbreviations are used in this manuscript:

2D	Two-Dimensional
3D	Three-Dimensional
CVT	Centroidal Voronoi Tessellation
FEA	finite-element analysis
GO	graphene oxide
PVC	polyvinyl chloride
RVE	representative volume element

## References

1. Ritchie, R.O.; Buehler, M.J.; Hansma, P. Plasticity and toughness in bone. *Phys. Today* **2009**, *62*, 41–47. [[CrossRef](#)]
2. Jäger, I.; Fratzl, P. Mineralized collagen fibrils: A mechanical model with a staggered arrangement of mineral particles. *Biophys. J.* **2000**, *79*, 1737–1746. [[CrossRef](#)] [[PubMed](#)]
3. Barthelat, F.; Tang, H.; Zavattieri, P.; Li, C.M.; Espinosa, H. On the mechanics of mother-of-pearl: A key feature in the material hierarchical structure. *J. Mech. Phys. Solids* **2007**, *55*, 306–337. [[CrossRef](#)]
4. Weiner, S.; Addadi, L. Design strategies in mineralized biological materials. *J. Mater. Chem.* **1997**, *7*, 689–702. [[CrossRef](#)]
5. Jackson, A.; Vincent, J.F.; Turner, R. The mechanical design of nacre. *Proc. R. Soc. Lond. Ser. B. Biol. Sci.* **1988**, *234*, 415–440.
6. Barthelat, F. Designing nacre-like materials for simultaneous stiffness, strength and toughness: Optimum materials, composition, microstructure and size. *J. Mech. Phys. Solids* **2014**, *73*, 22–37. [[CrossRef](#)]

7. Guo, X.; Gao, H. Bio-inspired material design and optimization. In *IUTAM Symposium on Topological Design Optimization of Structures, Machines and Materials: Status and Perspectives*; Springer: Berlin/Heidelberg, Germany, 2006; pp. 439–453.
8. Rabiei, R.; Bekah, S.; Barthelat, F. Failure mode transition in nacre and bone-like materials. *Acta Biomater.* **2010**, *6*, 4081–4089. [[CrossRef](#)] [[PubMed](#)]
9. Begley, M.R.; Philips, N.R.; Compton, B.G.; Wilbrink, D.V.; Ritchie, R.O.; Utz, M. Micromechanical models to guide the development of synthetic ‘brick and mortar’ composites. *J. Mech. Phys. Solids* **2012**, *60*, 1545–1560. [[CrossRef](#)]
10. Barthelat, F.; Mirkhalaf, M. The quest for stiff, strong and tough hybrid materials: An exhaustive exploration. *J. R. Soc. Interface* **2013**, *10*, 20130711. [[CrossRef](#)] [[PubMed](#)]
11. Bonderer, L.J.; Studart, A.R.; Gauckler, L.J. Bioinspired design and assembly of platelet reinforced polymer films. *Science* **2008**, *319*, 1069–1073. [[CrossRef](#)] [[PubMed](#)]
12. Valashani, S.M.M.; Barrett, C.J.; Barthelat, F. Self-assembly of microscopic tablets within polymeric thin films: A possible pathway towards new hybrid materials. *RSC Adv.* **2015**, *5*, 4780–4787. [[CrossRef](#)]
13. Deville, S.; Saiz, E.; Nalla, R.K.; Tomsia, A.P. Freezing as a path to build complex composites. *Science* **2006**, *311*, 515–518. [[CrossRef](#)] [[PubMed](#)]
14. Mao, L.B.; Gao, H.L.; Yao, H.B.; Liu, L.; Cölfen, H.; Liu, G.; Chen, S.M.; Li, S.K.; Yan, Y.X.; Liu, Y.Y.; et al. Synthetic nacre by pre-designed matrix-directed mineralization. *Science* **2016**, *354*, 107–110. [[CrossRef](#)] [[PubMed](#)]
15. Barthelat, F.; Zhu, D. A novel biomimetic material duplicating the structure and mechanics of natural nacre. *J. Mater. Res.* **2011**, *26*, 1203–1215. [[CrossRef](#)]
16. Espinosa, H.D.; Juster, A.L.; Latourte, F.J.; Loh, O.Y.; Gregoire, D.; Zavattieri, P.D. Tablet-level origin of toughening in abalone shells and translation to synthetic composite materials. *Nat. Commun.* **2011**, *2*, 173. [[CrossRef](#)] [[PubMed](#)]
17. Chintapalli, R.K.; Breton, S.; Dastjerdi, A.K.; Barthelat, F. Strain rate hardening: A hidden but critical mechanism for biological composites? *Acta Biomater.* **2014**, *10*, 5064–5073. [[CrossRef](#)] [[PubMed](#)]
18. Valashani, S.M.M.; Barthelat, F. A laser-engraved glass duplicating the structure, mechanics and performance of natural nacre. *Bioinspiration Biomim.* **2015**, *10*, 026005. [[CrossRef](#)] [[PubMed](#)]
19. Barthelat, F.; Rabiei, R. Toughness amplification in natural composites. *J. Mech. Phys. Solids* **2011**, *59*, 829–840. [[CrossRef](#)]
20. Barthelat, F.; Yin, Z.; Buehler, M.J. Structure and mechanics of interfaces in biological materials. *Nat. Rev. Mater.* **2016**, *1*, 1–16. [[CrossRef](#)]
21. Kotha, S.; Li, Y.; Guzelsu, N. Micromechanical model of nacre tested in tension. *J. Mater. Sci.* **2001**, *36*, 2001–2007. [[CrossRef](#)]
22. Bar-On, B.; Wagner, H.D. Mechanical model for staggered bio-structure. *J. Mech. Phys. Solids* **2011**, *59*, 1685–1701. [[CrossRef](#)]
23. Gao, H. Application of fracture mechanics concepts to hierarchical biomechanics of bone and bone-like materials. *Int. J. Fract.* **2006**, *138*, 101–137. [[CrossRef](#)]
24. Alava, M.J.; Nukala, P.K.; Zapperi, S. Statistical models of fracture. *Adv. Phys.* **2006**, *55*, 349–476. [[CrossRef](#)]
25. Dimas, L.S.; Giesa, T.; Buehler, M.J. Coupled continuum and discrete analysis of random heterogeneous materials: Elasticity and fracture. *J. Mech. Phys. Solids* **2014**, *63*, 481–490. [[CrossRef](#)]
26. Katti, D.R.; Katti, K.S. Modeling microarchitecture and mechanical behavior of nacre using 3D finite element techniques Part I Elastic properties. *J. Mater. Sci.* **2001**, *36*, 1411–1417. [[CrossRef](#)]
27. Askarnejad, S.; Rahbar, N. Toughening mechanisms in bioinspired multilayered materials. *J. R. Soc. Interface* **2015**, *12*, 20140855. [[CrossRef](#)] [[PubMed](#)]
28. Pro, J.W.; Lim, R.K.; Petzold, L.R.; Utz, M.; Begley, M.R. GPU-based simulations of fracture in idealized brick and mortar composites. *J. Mech. Phys. Solids* **2015**, *80*, 68–85.
29. Pro, J.W.; Lim, R.K.; Petzold, L.R.; Utz, M.; Begley, M.R. The impact of stochastic microstructures on the macroscopic fracture properties of brick and mortar composites. *Extrem. Mech. Lett.* **2015**, *5*, 1–9. [[CrossRef](#)]
30. Mirkhalaf, M.; Barthelat, F. Nacre-like materials using a simple doctor blading technique: Fabrication, testing and modeling. *J. Mech. Behav. Biomed. Mater.* **2016**, *56*, 23–33. [[CrossRef](#)] [[PubMed](#)]
31. Niebel, T.P.; Bouville, F.; Kokkinis, D.; Studart, A.R. Role of the polymer phase in the mechanics of nacre-like composites. *J. Mech. Phys. Solids* **2016**, *96*, 133–146. [[CrossRef](#)]
32. Anup, S. Influence of initial flaws on the mechanical properties of nacre. *J. Mech. Behav. Biomed. Mater.* **2015**, *46*, 168–175. [[CrossRef](#)] [[PubMed](#)]
33. Chandler, M.Q.; Cheng, J.R.C. Discrete element modeling of microstructure of nacre. *Comput. Part. Mech.* **2018**, *5*, 191–201. [[CrossRef](#)]
34. Lim, R.K.; Pro, J.W.; Begley, M.R.; Utz, M.; Petzold, L.R. High-performance simulation of fracture in idealized ‘brick and mortar’ composites using adaptive Monte Carlo minimization on the GPU. *Int. J. High Perform. Comput. Appl.* **2016**, *30*, 186–199. [[CrossRef](#)]
35. Gao, H.; Ji, B.; Jäger, I.L.; Arzt, E.; Fratzl, P. Materials become insensitive to flaws at nanoscale: Lessons from nature. *Proc. Natl. Acad. Sci. USA* **2003**, *100*, 5597–5600. [[CrossRef](#)] [[PubMed](#)]
36. Tran, P.; Ngo, T.D.; Ghazlan, A.; Hui, D. Bimaterial 3D printing and numerical analysis of bio-inspired composite structures under in-plane and transverse loadings. *Compos. Part B Eng.* **2017**, *108*, 210–223. [[CrossRef](#)]
37. Maghsoudi-Ganjeh, M.; Lin, L.; Yang, X.; Zeng, X. Computational modeling and simulation of bioinspired nacre-like composites. *J. Mater. Res.* **2021**, *36*, 2651–2661. [[CrossRef](#)]

38. Lin, L.; Wang, X.; Zeng, X. Computational modeling of interfacial behaviors in nanocomposite materials. *Int. J. Solids Struct.* **2017**, *115*, 43–52. [[CrossRef](#)] [[PubMed](#)]
39. Lin, L.; Wang, X.; Zeng, X. Geometrical modeling of cell division and cell remodeling based on Voronoi tessellation method. *CMES Comput. Model. Eng. Sci.* **2014**, *98*, 203–220.
40. Evesque, P.; Adjémian, F. Stress fluctuations and macroscopic stick-slip in granular materials. *Eur. Phys. J. E* **2002**, *9*, 253–259. [[CrossRef](#)] [[PubMed](#)]
41. Dastjerdi, A.K.; Rabiei, R.; Barthelat, F. The weak interfaces within tough natural composites: Experiments on three types of nacre. *J. Mech. Behav. Biomed. Mater.* **2013**, *19*, 50–60. [[CrossRef](#)] [[PubMed](#)]
42. Barthelat, F.; Espinosa, H. An experimental investigation of deformation and fracture of nacre–other of pearl. *Exp. Mech.* **2007**, *47*, 311–324. [[CrossRef](#)]
43. Barthelat, F.; Li, C.M.; Comi, C.; Espinosa, H.D. Mechanical properties of nacre constituents and their impact on mechanical performance. *J. Mater. Res.* **2006**, *21*, 1977–1986. [[CrossRef](#)]
44. Lopez, M.I.; Martinez, P.E.M.; Meyers, M.A. Organic interlamellar layers, mesolayers and mineral nanobridges: Contribution to strength in abalone (*Haliotis rufescence*) nacre. *Acta Biomater.* **2014**, *10*, 2056–2064. [[CrossRef](#)] [[PubMed](#)]
45. Song, F.; Soh, A.; Bai, Y. Structural and mechanical properties of the organic matrix layers of nacre. *Biomaterials* **2003**, *24*, 3623–3631. [[CrossRef](#)] [[PubMed](#)]
46. Wang, R.; Suo, Z.; Evans, A.; Yao, N.; Aksay, I. Deformation mechanisms in nacre. *J. Mater. Res.* **2001**, *16*, 2485–2493. [[CrossRef](#)]
47. Meyers, M.A.; McKittrick, J.; Chen, P.Y. Structural biological materials: Critical mechanics–materials connections. *Science* **2013**, *339*, 773–779. [[CrossRef](#)] [[PubMed](#)]
48. Lin, L.; Zeng, X. Numerical investigation of the role of intercellular interactions on collective epithelial cell migration. *Biomech. Model. Mechanobiol.* **2018**, *17*, 439–448. [[CrossRef](#)] [[PubMed](#)]
49. Maghsoudi-Ganjeh, M.; Lin, L.; Wang, X.; Wang, X.; Zeng, X. Computational modeling of the mechanical behavior of 3D hybrid organic–inorganic nanocomposites. *JOM* **2019**, *71*, 3951–3961. [[CrossRef](#)]
50. Maghsoudi-Ganjeh, M.; Wang, X.; Zeng, X. Computational investigation of the effect of water on the nanomechanical behavior of bone. *J. Mech. Behav. Biomed. Mater.* **2020**, *101*, 103454. [[CrossRef](#)] [[PubMed](#)]
51. Maghsoudi-Ganjeh, M.; Lin, L.; Wang, X.; Zeng, X. Computational investigation of ultrastructural behavior of bone using a cohesive finite element approach. *Biomech. Model. Mechanobiol.* **2019**, *18*, 463–478. [[CrossRef](#)]
52. Maghsoudi-Ganjeh, M.; Lin, L.; Wang, X.; Zeng, X. Bioinspired design of hybrid composite materials. *Int. J. Smart Nano Mater.* **2019**, *10*, 90–105. [[CrossRef](#)]
53. Lin, L.; Wang, X.; Zeng, X. An improved interfacial bonding model for material interface modeling. *Eng. Fract. Mech.* **2017**, *169*, 276–291. [[CrossRef](#)] [[PubMed](#)]
54. Smith, B.L.; Schäffer, T.E.; Viani, M.; Thompson, J.B.; Frederick, N.A.; Kindt, J.; Belcher, A.; Stucky, G.D.; Morse, D.E.; Hansma, P.K. Molecular mechanistic origin of the toughness of natural adhesives, fibres and composites. *Nature* **1999**, *399*, 761–763. [[CrossRef](#)]
55. Evans, A.; Suo, Z.; Wang, R.; Aksay, I.; He, M.; Hutchinson, J. Model for the robust mechanical behavior of nacre. *J. Mater. Res.* **2001**, *16*, 2475–2484. [[CrossRef](#)]
56. Lin, A.Y.M.; Meyers, M.A.M. Interfacial shear strength in abalone nacre. *J. Mech. Behav. Biomed. Mater.* **2009**, *2*, 607–612. [[CrossRef](#)] [[PubMed](#)]
57. Espinosa, H.D.; Rim, J.E.; Barthelat, F.; Buehler, M.J. Merger of structure and material in nacre and bone—respectives on de novo biomimetic materials. *Prog. Mater. Sci.* **2009**, *54*, 1059–1100. [[CrossRef](#)]
58. Hrabánková, I.; Frýda, J.; Šepitka, J.; Sasaki, T.; Frýdová, B.; Lukeš, J. Mechanical properties of deep-sea molluscan shell. *Comput. Methods Biomech. Biomed. Eng.* **2013**, *16*, 287–289. [[CrossRef](#)] [[PubMed](#)]
59. Zhang, N.; Chen, Y. Nanoscale plastic deformation mechanism in single crystal aragonite. *J. Mater. Sci.* **2013**, *48*, 785–796. [[CrossRef](#)]
60. Hughes, T.J.; Pister, K.S.; Taylor, R.L. Implicit-explicit finite elements in nonlinear transient analysis. *Comput. Methods Appl. Mech. Eng.* **1979**, *17*, 159–182. [[CrossRef](#)]
61. Ni, Y.; Song, Z.; Jiang, H.; Yu, S.H.; He, L. Optimization design of strong and tough nacreous nanocomposites through tuning characteristic lengths. *J. Mech. Phys. Solids* **2015**, *81*, 41–57. [[CrossRef](#)]
62. Wu, K.; Zheng, Z.; Zhang, S.; He, L.; Yao, H.; Gong, X.; Ni, Y. Interfacial strength-controlled energy dissipation mechanism and optimization in impact-resistant nacreous structure. *Mater. Des.* **2019**, *163*, 107532. [[CrossRef](#)]
63. Gao, H.L.; Chen, S.M.; Mao, L.B.; Song, Z.Q.; Yao, H.B.; Cölfen, H.; Luo, X.S.; Zhang, F.; Pan, Z.; Meng, Y.F.; et al. Mass production of bulk artificial nacre with excellent mechanical properties. *Nat. Commun.* **2017**, *8*, 287. [[CrossRef](#)] [[PubMed](#)]
64. Moheimani, R.; Sarayloo, R.; Dalir, H. Failure study of fiber/epoxy composite laminate interface using cohesive multiscale model. *Adv. Compos. Lett.* **2020**, *29*, 2633366X20910157. [[CrossRef](#)]
65. Keshavanarayana, S.R.; Shahverdi, H.; Kothare, A.; Yang, C.; Bingenheimer, J. The effect of node bond adhesive fillet on uniaxial in-plane responses of hexagonal honeycomb core. *Compos. Struct.* **2017**, *175*, 111–122. [[CrossRef](#)]
66. Ehsani, A.; Rezaeepazhand, J. Stacking sequence optimization of laminated composite grid plates for maximum buckling load using genetic algorithm. *Int. J. Mech. Sci.* **2016**, *119*, 97–106. [[CrossRef](#)]
67. Song, J.; Fan, C.; Ma, H.; Liang, L.; Wei, Y. Crack deflection occurs by constrained microcracking in nacre. *Acta Mech. Sin.* **2017**, *34*, 143–150. [[CrossRef](#)]

68. Liu, J.; Xu, Y.; Yang, H.; Liu, Y.; Yarlagadda, P.K.; Yan, C. Investigation of failure mechanisms of nacre at macro and nano scales. *J. Mech. Behav. Biomed. Mater.* **2020**, *112*, 104018. [[CrossRef](#)] [[PubMed](#)]
69. Liang, S.M.; Ji, H.M.; Li, X.W. The crucial role of platelet stacking mode in strength and toughness of nacre. *Mater. Des.* **2023**, *230*, 111987. [[CrossRef](#)]
70. Cui, W.; Li, M.; Liu, J.; Wang, B.; Zhang, C.; Jiang, L.; Cheng, Q. A strong integrated strength and toughness artificial nacre based on dopamine cross-linked graphene oxide. *ACS Nano* **2014**, *8*, 9511–9517. [[CrossRef](#)] [[PubMed](#)]
71. Kwon, Y.B.; Lee, S.R.; Seo, T.H.; Kim, Y.K. Fabrication of a strong artificial nacre based on tannic acid-functionalized graphene oxide and poly (vinyl alcohol) through their multidentate hydrogen bonding. *Macromol. Res.* **2022**, *30*, 279–284. [[CrossRef](#)]
72. Wang, Y.; Li, T.; Ma, P.; Zhang, S.; Zhang, H.; Du, M.; Xie, Y.; Chen, M.; Dong, W.; Ming, W. Artificial nacre from supramolecular assembly of graphene oxide. *ACS Nano* **2018**, *12*, 6228–6235. [[CrossRef](#)] [[PubMed](#)]
73. Song, P.; Xu, Z.; Wu, Y.; Cheng, Q.; Guo, Q.; Wang, H. Super-tough artificial nacre based on graphene oxide via synergistic interface interactions of  $\pi$ - $\pi$  stacking and hydrogen bonding. *Carbon* **2017**, *111*, 807–812. [[CrossRef](#)]
74. Tang, S.; Wu, Z.; Li, X.; Xie, F.; Ye, D.; Ruiz-Hitzky, E.; Wei, L.; Wang, X. Nacre-inspired biodegradable nanocellulose/MXene/AgNPs films with high strength and superior gas barrier properties. *Carbohydr. Polym.* **2023**, *299*, 120204. [[CrossRef](#)] [[PubMed](#)]
75. Liu, Z.; Wang, W.; Tan, J.; Liu, J.; Zhu, M.; Zhu, B.; Zhang, Q. Bioinspired ultra-thin polyurethane/MXene nacre-like nanocomposite films with synergistic mechanical properties for electromagnetic interference shielding. *J. Mater. Chem. C* **2020**, *8*, 7170–7180. [[CrossRef](#)]
76. Wang, J.; Song, T.; Ming, W.; Yele, M.; Chen, L.; Zhang, H.; Zhang, X.; Liang, B.; Wang, G. High MXene loading, nacre-inspired MXene/ANF electromagnetic interference shielding composite films with ultralong strain-to-failure and excellent Joule heating performance. *Nano Res.* **2024**, *17*, 2061–2069. [[CrossRef](#)]
77. Wang, H.; Wang, Y.; Chang, J.; Yang, J.; Dai, H.; Xia, Z.; Hui, Z.; Wang, R.; Huang, W.; Sun, G. Nacre-inspired strong MXene/cellulose fiber with superior supercapacitive performance via synergizing the interfacial bonding and interlayer spacing. *Nano Lett.* **2023**, *23*, 5663–5672. [[CrossRef](#)] [[PubMed](#)]
78. Wang, H.; Lu, R.; Yan, J.; Peng, J.; Tomsia, A.P.; Liang, R.; Sun, G.; Liu, M.; Jiang, L.; Cheng, Q. Tough and conductive nacre-inspired MXene/epoxy layered bulk nanocomposites. *Angew. Chem. Int. Ed.* **2023**, *62*, e202216874. [[CrossRef](#)] [[PubMed](#)]
79. Gao, D.; Chen, P.; Zhao, Y.; Lu, G.; Yang, H. Physical Mechanism and Resistance Characteristics of Nacre-Like Composites for Two-Point Impact. *J. Mater. Eng. Perform.* **2023**, 1–18. [[CrossRef](#)]
80. Gao, D.; Chen, P.; Lu, G.; Yang, H. Numerical analysis for impact resistance of nacre-like composites. *Mater. Today Commun.* **2023**, *35*, 106031. [[CrossRef](#)]
81. Flores-Johnson, E.; Shen, L.; Guiamatsia, I.; Nguyen, G.D. Numerical investigation of the impact behaviour of bioinspired nacre-like aluminium composite plates. *Compos. Sci. Technol.* **2014**, *96*, 13–22. [[CrossRef](#)]

**Disclaimer/Publisher’s Note:** The statements, opinions and data contained in all publications are solely those of the individual author(s) and contributor(s) and not of MDPI and/or the editor(s). MDPI and/or the editor(s) disclaim responsibility for any injury to people or property resulting from any ideas, methods, instructions or products referred to in the content.